

## Research Article

# Nanostructured CeO<sub>2</sub> Thin Films Prepared by the Sol-Gel Dip-Coating Method with Anomalous Behavior of Crystallite Size and Bandgap

Y. J. Acosta-Silva,<sup>1</sup> M. Toledano-Ayala,<sup>1</sup> G. Torres-Delgado,<sup>2</sup> I. Torres-Pacheco,<sup>1</sup>  
A. Méndez-López ,<sup>1</sup> R. Castanedo-Pérez,<sup>2</sup> and O. Zelaya-Ángel<sup>3</sup>

<sup>1</sup>División de Investigación y Posgrado, Facultad de Ingeniería, Universidad Autónoma de Querétaro (UAQ), Centro Universitario, Qro., 76010 Querétaro, Mexico

<sup>2</sup>Centro de Investigación y de Estudios Avanzados del I.P.N., Unidad Querétaro, 76230 Querétaro, Querétaro, Mexico

<sup>3</sup>Depto. de Física, Centro de Investigación y de Estudios Avanzados del I.P.N., A.P. 14-740, Ciudad de México 07360, Mexico

Correspondence should be addressed to A. Méndez-López; [arturo.mendez@uaq.mx](mailto:arturo.mendez@uaq.mx)

Received 11 June 2019; Revised 23 July 2019; Accepted 10 August 2019; Published 31 October 2019

Academic Editor: Oscar Perales-Pérez

Copyright © 2019 Y. J. Acosta-Silva et al. This is an open access article distributed under the Creative Commons Attribution License, which permits unrestricted use, distribution, and reproduction in any medium, provided the original work is properly cited.

Amorphous CeO<sub>2</sub> thin films were deposited by a dip-coating method on Corning glass substrates and annealed for one hour at the temperatures ( $T$ ) of 250, 450, and 550°C in air for crystallization. The precursor solution was prepared by dissolving cerium acetate in methanol, lactic acid, glycerol, and trimethylamine at 55°C. X-ray diffraction (XRD) patterns showed the cubic structure of CeO<sub>2</sub>. From XRD data and employing the Scherrer formula, the crystallite size (CS) was calculated to be within the  $4.0 \pm 0.5$  to  $10 \pm 1$  nm interval. SEM micrographs revealed cracks of the films annealed at 250 and 450°C, even though for 550°C, the film shows a homogeneous morphology free of cracks. CS increases (from 4.0 to 10 nm) and thickness decreases (from 217 to 182 nm) when  $T$  increases. The UV-vis spectra exhibited an average transmittance of 80% in the 300 to 2000 nm wavelength range. Also, from XRD, it was observed that the lattice shrinks and from transmittance that the bandgap energy increases with  $T$ . The Raman spectra exhibit  $461 \text{ cm}^{-1}$  assigned to F<sub>2g</sub> mode of the fluorite cubic structure, where F<sub>2g</sub> hardens when  $T$  increases as an effect of the shrinkage of the lattice.

## 1. Introduction

Cerium dioxide is one of the most abundant rare earth that have attracted attention due to its interesting properties that include chemical stability, high values for the refractive index, optical transparency in the visible region, and hardness [1, 2]. This oxide has a wide versatility for its multiple properties adequate for many industrial applications, which can be an appropriate substitute of ZnO and TiO<sub>2</sub> [3, 4]. The CeO<sub>2</sub> is stable even in the substoichiometric form (CeO<sub>2-x</sub>,  $0 < x < 0.4$ ) and thus has been easily produced by several deposition techniques [5]. The CeO<sub>2</sub> thin films have been used in different applications such as solar energy conversion [6], gas sensors [7], catalysis [8], and corrosion-resistant and protective coatings [9]. The CeO<sub>2</sub> thin films

can be prepared by several methods such as pulsed laser deposition (PLD) [10], magnetron sputtering [11], spray pyrolysis [12, 13], and chemical vapor deposition (CVD) [14]. Another critical topic apart from the deposit techniques is the first-principles calculations of different materials. Goyenola et al. [15] have made recent studies. However, most of these preparation methods require a large amount of energy, complex devices, and vacuum during film deposition. The sol-gel dip-coating technique is simple and economical; the possibility to process at low temperature, large surface area coatings, and substrates with complex shapes can be used. Also, films with crystalline quality, chemical stability, and high optical transmission can be obtained [16, 17].

On the other hand, the CeO<sub>2</sub> films are usually synthesized by the sol-gel method using cerium chloride or cerium

nitrate as the precursor and citric acid as the stabilizer. Wang et al. [18] reported the synthesis of CeO<sub>2</sub> films by the sol-gel method using cerium nitrate as the precursor and citric acid as the chelating agent, and they also studied the effect of annealing temperature on oxygen vacancies. Verma et al. [19] prepared CeO<sub>2</sub> films with cerium chloride heptahydrate (0.22 M) and citric acid with different molar ratios; the addition of citric acid to the precursor leads to homogeneity and a reduced ion storage capacity in the films. Škofic et al. [20] also reported the synthesis of CeO<sub>2</sub> films using cerium chloride heptahydrate in a mixture of citric acid and ethanol, where the films were heat-treated in an air or argon atmosphere. The structural, electrochemical, and optical properties of these films depended on the preparation conditions.

In the present work, thin films of CeO<sub>2</sub> were synthesized by the sol-gel dip-coating method; the precursor solution was prepared using cerium acetate as the precursor and lactic acid as the stabilizer. The films were analyzed by X-ray diffraction (XRD), Raman spectroscopy, UV and visible spectroscopy (UV-vis), and scanning electron microscopy (SEM). In the characterization, the effect of the annealing temperature on the structural, optical, and morphology properties of CeO<sub>2</sub> thin films was studied, where it was found that stress induced by oxygen vacancies (VOs) prevails on the quantum confinement effect. To know the way of how VOs affect the lattice by considering the quantum confinement and strain requires first-principles studies at nanometric dimensions, similar to the work carried out by Goyenola et al. in fullerene-like CS<sub>x</sub> [15]. In this sense, it is worth mentioning that Kossoy and coworkers have associated elastic anomalies to stress due to VOs in CeO<sub>2</sub> [21]. These anomalies can produce desirable or undesirable effects in the material since affecting the band structure and, hence, the optical properties [22]. Besides, the application of ferromagnetic semiconductor and oxides as the material base for spintronics has stimulated the search of these types of materials. Recent works report that strain induces ferromagnetism in semiconductors and oxides [23], such is the case of ferromagnetism induced in Nd-doped CeO<sub>2</sub> nanoparticles due to VOs provoked by the doping [24].

## 2. Experimental

The CeO<sub>2</sub> thin films were prepared by the sol-gel dip-coating method. The precursor solution was prepared by dissolving 1 mol of cerium acetate (Ce(CH<sub>3</sub>CO<sub>2</sub>)<sub>3</sub>·xH<sub>2</sub>O) in 100 mol of methanol; after that, 1.5 mol of lactic acid, 0.2 mol of glycerol, and 1 mol of trimethylamine were added to the solution at 55°C and kept under stirring conditions for 1 hour. Finally, the precursor solution was cooled at room temperature. Thin films were deposited by the dip-coating method on glass substrates, and withdrawal speed of 10.0 cm/min was used; the surrounding relative humidity during the film removal was lower than 30%. The dip-coating process was applied eight times; after each coat, the film was dried at 250°C for 5 min; when the cycle was completed, the films were dried at 250°C for 1 hour in air and afterward sintered at different temperatures (*T*) (250, 450, and 550°C) for 1 h. The phase of the CeO<sub>2</sub> thin films was determined using a Rigaku D/max-2100 diffractometer (Cu *k*α radiation, 1.5406 Å) in the range

of 20–90° for an incidence angle of 0.5°. The crystallite size was calculated employing the Scherrer equation. Structural properties were also studied by Raman spectroscopy. Raman spectra were measured at room temperature in a wavelength range between 300 and 700 nm using a Labram-Dilor Raman spectrometer, with a He-Ne laser as the exciting source. The morphology and thickness of the films were studied by scanning electron microscopy using an XL 30ESEM Philips microscope at 50000x. Optical transmittance was measured with a Cary 5000 UV-vis-NIR spectrophotometer in the 200–1000 nm range. The surface roughness of the films was measured by using an atomic force microscope (AFM), Park Scientific Inst. System.

## 3. Results and Discussion

### 3.1. Structural Properties

**3.1.1. X-Ray Diffraction (XRD).** X-ray diffraction (XRD) patterns of the films for different annealing temperatures are displayed in Figure 1. The XRD pattern for the film annealed at 550°C presents peaks at 28.54°, 33.07°, 47.48°, 56.34°, 59.09°, 69.41°, 76.70°, 79.07°, and 88.42° corresponding to the planes (111), (200), (220), (311), (222), (400), (331), (420), and (422), respectively, which are in good agreement with JCPDS card No. 43-1002 of the fluorite cubic structure. For the diffraction patterns of the films annealed at 250 and 450°C, the absence of some diffraction peaks suggests a decreasing in crystallinity. The left inset of Figure 1 exhibits the shift toward larger 2θ of the (111) diffraction values when *T* increases. This behavior, in turn, indicates that the lattice shrinks, as observed in the right inset where the (111) and (002) interplanar spacings (ISs) are plotted as a function of *T*, and how both ISs decrease when *T* rises. The decreasing of the interplanar spacings is originated by strain provoked by the creation of VOs.

**3.1.2. Crystallite Size and Thickness.** Figure 2 illustrates the variation of the thickness, measured from SEM images, with *T* (left axis). The decreasing of the thickness when *T* increases suggests that, since the nonannealed films were pieces of the same sample, the CeO<sub>2</sub> lattice shrinks probably due to the VO formation, in such a way that more temperature equals larger desorption of oxygen. The crystallite size (CS) of the CeO<sub>2</sub> films was calculated from the (111) and (002) diffraction peaks using Scherrer's equation ( $D = 0.9\lambda/\beta \cos \theta$ ), where the shape factor *K* is 0.9, λ = 1.540598 Å, β is the full width at half maximum (FWHM) of the (111) peak, and θ is Bragg's angle [25]. Figure 2 (right axis) displays the CS dependence with the annealing temperature; observe that two different values of CS were obtained from the two peaks; the asterisks indicate mean values. Larger CS generally corresponds to better crystallinity; thus, CeO<sub>2</sub> films annealed at 550°C got the best crystalline quality. The average crystallite size of the CeO<sub>2</sub> films was found to be in the range 4.0 ± 0.5 to 11.0 ± 1 nm, which agrees with films synthesized by the sol-gel method [18]. Strain alters the real value of CS [15]; Figure 2 shows that CS values calculated depend on the

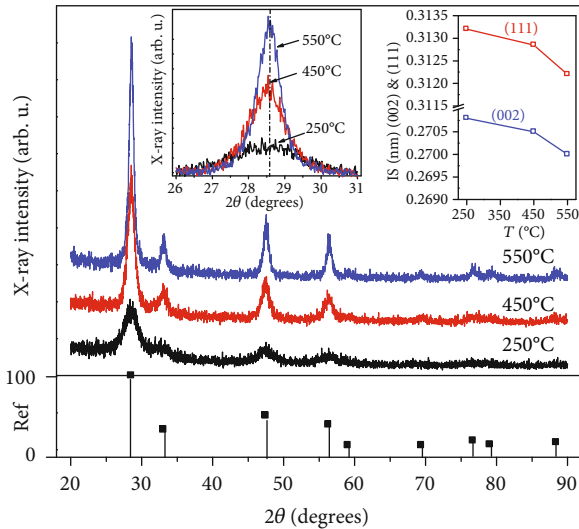


FIGURE 1: XRD patterns of the  $\text{CeO}_2$  films annealed at different temperatures. The left inset shows the shift toward larger  $2\theta$  values of the (111) reflection when  $T$  increases. The right inset exhibits how the interplanar spacing (IS) of lattice along the (111) and (002) directions shrinks with  $T$ .

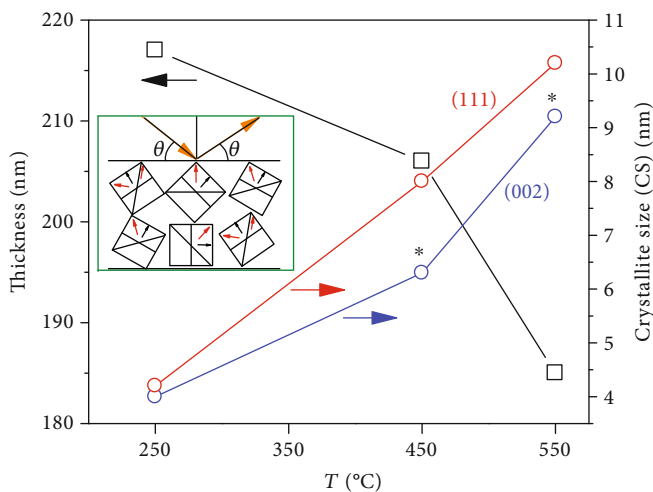


FIGURE 2: Thickness (left axis) and crystallite size (CS) (right axis) versus  $T$ . Red and blue lines indicate CS measured from (111) and (002) peaks. The inset illustrates a cartoon in which crystallites of the  $\text{CeO}_2$  films show a tendency to be with a preferred orientation along the (111) direction.

crystalline direction. The reason could be that, as can be observed in XRD patterns of Figure 1, the films show a certain grade of preferred orientation along the (111) direction, which is where CS is measured. Consequently, due to the free surface of the films, the strain is larger than that on the (002) that have more projection to the substrate (see inset of Figure 2) which opposes the strain. This effect is also observed in the IS of the right inset of Figure 1.

### 3.2. Morphological Properties

**3.2.1. Scanning Electron Microscopy (SEM).** The morphology of the films was also determined by scanning electron microscopy. The surface morphology of the  $\text{CeO}_2$  films annealed at 250°C, 450°C, and 550°C is shown in Figures 3(a)–3(c). The SEM image of the  $\text{CeO}_2$  annealed at 250°C shows an extensive cracking. This is probably due to shrinkage of the film upon drying [26]. Other reasons for cracks might be the internal stress [9]; also, the withdrawing speed is too high [27]. Similar results were reported by Carvalho et al. [9], Mihalache and Pasuk [27], and Suresh et al. [28]. The SEM image of the  $\text{CeO}_2$  film annealed at 550°C presents a film with homogeneous morphology and free of cracks.

AFM images also indicate that the changes of surface morphology and roughness of  $\text{CeO}_2$  thin films were highly dependent on  $T$ . SEM images of cross-sections of the films also allow to measure the thickness. Figure 4 shows the thickness of the  $\text{CeO}_2$  films annealed at 450°C (Figure 4(a)) and 550°C (Figure 4(b)). The micrographs clearly show a decreasing in thickness with the increasing of  $T$ . Similar results were reported by Suresh et al. [28].

**3.2.2. Atomic Force Microscopy (AFM).** The surface morphology of the  $\text{CeO}_2$  thin films was also investigated by atomic force microscopy (AFM). Figure 5 shows AFM 3D images of the  $\text{CeO}_2$  thin film morphology sintered at 250, 450, and 550°C, respectively. In Figure 5(a), the AFM image of the  $\text{CeO}_2$  thin film sintered at 250°C shows that the surface is smooth and uniform. When the sintering temperature is increased at 450 (Figure 5(b)) and 550°C, on the surface of films, sintered small grain agglomerates appear (Figure 5(c)) together and randomly distributed. The measured Root Mean Square (RMS) surface roughness of the  $\text{CeO}_2$  thin films sintered at 250, 450, and 550°C was 2.5, 3.5, and 6.0 nm, respectively.

### 3.3. Optical Properties

**3.3.1. Transmittance.** Figure 6 shows the transmission spectra of the  $\text{CeO}_2$  films annealed at different temperatures. All the sintered films have good transparency in the 400–2000 nm region. The transmittance reaches ~75% for the films annealed at 450 and 550°C. The energy bands of  $\text{CeO}_2$  can be split into two: the valence band derived from  $\text{O}2p$  states and the conduction band from the  $\text{Ce}5d$  states. In between lay the empty  $\text{Ce}4f$  states with a strong atomic-like character, leading to two bandgaps. Some works have been reported that explore the band structure, though not leading to precise values for these bandgaps, as pointed out by Castleton et al. [29]. However, the most common values reported are  $\text{O}2p \rightarrow \text{Ce}4f$  bandgap taken as 2.6–3.4 eV; 5.5–6.5 eV range is chosen for  $\text{O}2p \rightarrow \text{Ce}5d$  [30, 31].

UV-Vis spectra show a strong absorption band below 400 nm, that is, the absorption edge, due to the charge-transfer transition from  $\text{O}^{2-}$  (2p) to  $\text{Ce}^{4+}$  (4f) orbitals in  $\text{CeO}_2$  [32].

The values of both the direct ( $E_{gd}$ ) and indirect ( $E_{gi}$ ) optical bandgap energies were obtained from the linear fitting of the plot  $(\alpha h\nu)^2$  and  $(\alpha h\nu)^{1/2}$  vs. the photon energy

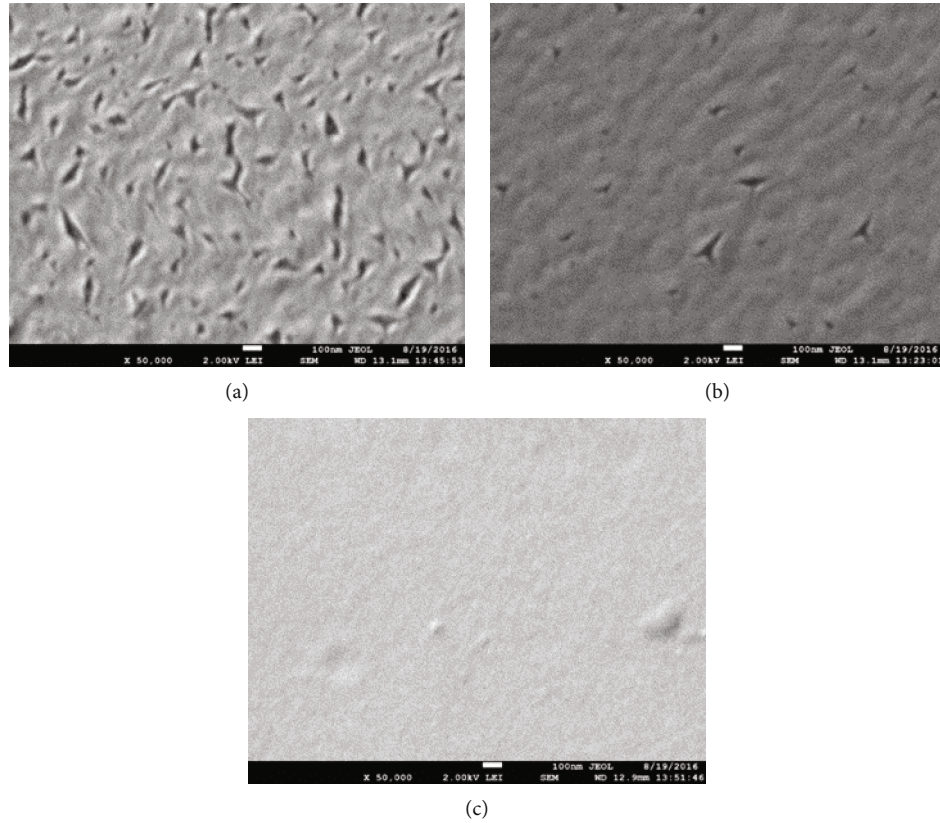


FIGURE 3:  $2.5 \mu\text{m} \times 2.5 \mu\text{m}$  SEM images (the white bar in the images is 100 nm) of the  $\text{CeO}_2$  films annealed at (a)  $250^\circ\text{C}$ , (b)  $450^\circ\text{C}$ , and (c)  $550^\circ\text{C}$ .

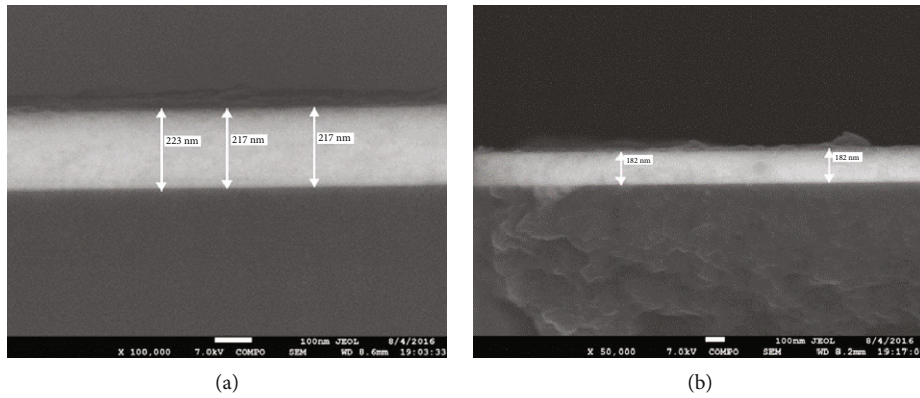


FIGURE 4: Micrographs of the thickness (the white bar in the images is 100 nm) of the  $\text{CeO}_2$  films annealed at 450 (a) and  $550^\circ\text{C}$  (b).

( $h\nu$ ), respectively (see Figure 7), where it can be observed how the linear fits for both  $E_{gD}$  and  $E_{gI}$  shift to higher energies with increasing  $T$ . The increment of  $E_{gI}$  bandgap when  $T$  rises has been reported by Zarkov and coworkers [33]. Figure 8 exhibits  $E_{gD}$  and  $E_{gI}$  versus  $T$ . The figure shows that both  $E_g$  values described, approximately, parallel line shapes, i.e., have the same energy separation in the  $250\text{--}550^\circ\text{C}$  interval of  $T$ . Since  $E_{gI} < E_{gD}$ , as expected for  $\text{CeO}_2$ , the bandgap is indirect. However, for the nanometric  $\text{CeO}_2$  dimensions, generally, the bandgap increases when the particle size decreases, due to quantum confinement effect. The *Bohr radius* of  $\text{CeO}_2$  is of

the order of  $7\text{--}8 \text{ nm}$  [34]; therefore, in our case, the quantum effects should strongly influence the results.

The decreasing of both bandgaps when the size of crystal size decreases could be related to the shrinkage of the lattice (see Figure 1), which introduces strong stress in the structure in such a way that its effect dominates the quantum confinement.

**3.3.2. Raman Spectroscopy.** The formation of a cubic structure in the  $\text{CeO}_2$  films was confirmed by Raman spectroscopy. Figure 9 shows the Raman spectra of the  $\text{CeO}_2$  films

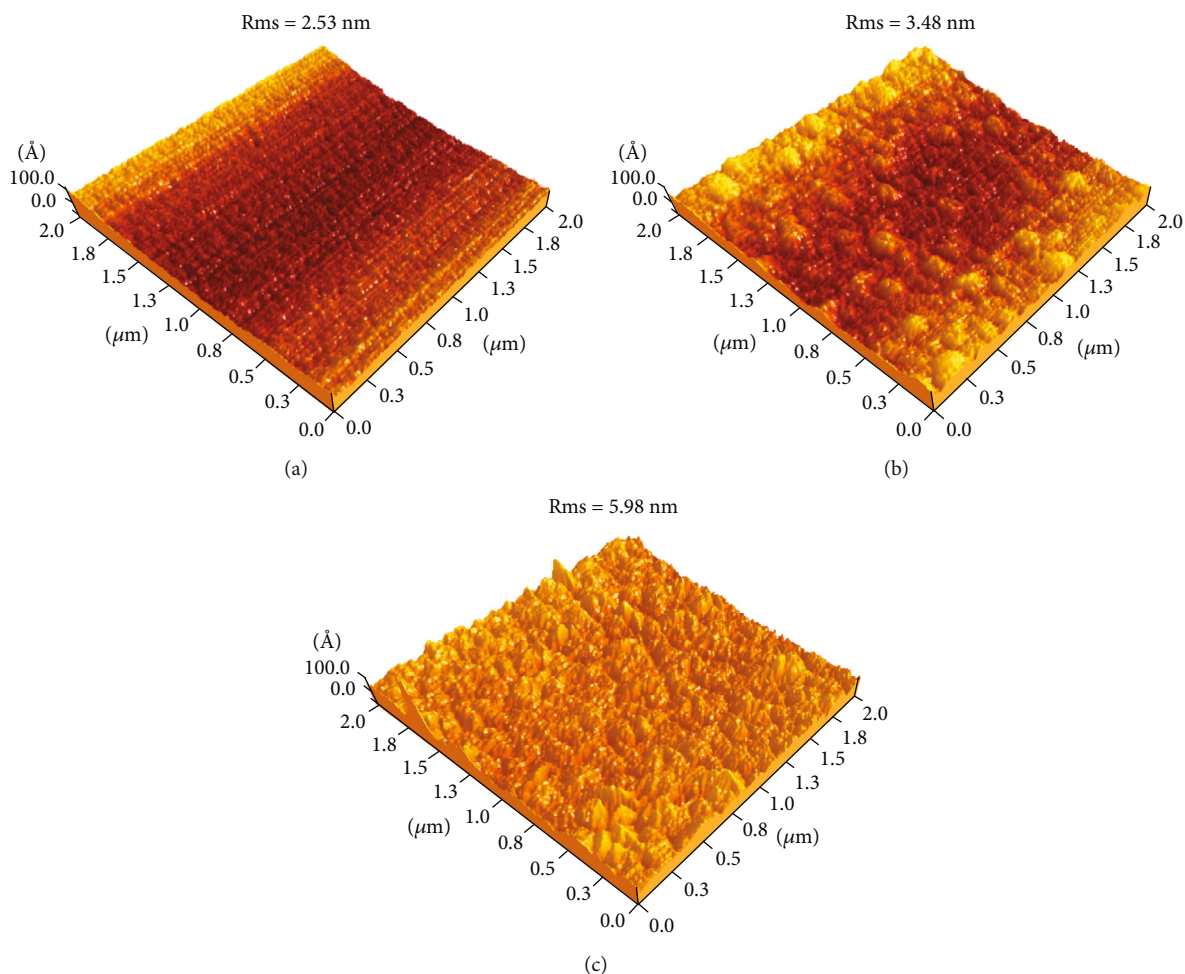


FIGURE 5: 3D images of  $\text{CeO}_2$  thin films sintered at different temperatures: (a)  $250^\circ\text{C}$ , (b)  $450^\circ\text{C}$ , and (c)  $550^\circ\text{C}$ .

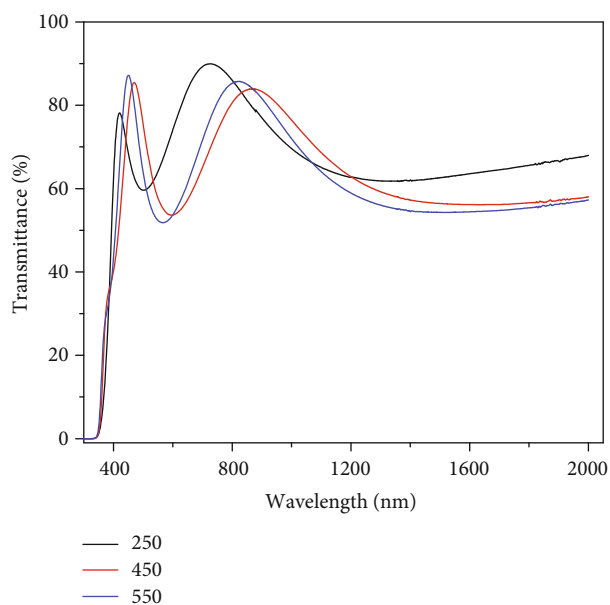


FIGURE 6: Transmission spectra of  $\text{CeO}_2$  thin films annealed at different temperatures.

annealed at different temperatures. The Raman spectra of the samples exhibit a Raman mode at  $461\text{ cm}^{-1}$  which has  $F_{2g}$  symmetry assigned to the cubic structure of the fluorite and can be viewed as a first-order symmetric stretching mode of the  $\text{Ce-O}_8$  vibrational units [35]. This mode should be very sensitive to any disorder in the oxygen sublattice resulting from thermal, doping, or crystal size [36], as can be observed on how the FWHM of the  $F_{2g}$  mode increases as the CS decreases in Figure 9. Hattori et al. [36] reported an increase of this peak with increasing heat treatment temperature from  $400$  to  $1000^\circ\text{C}$ . The bandwidth of this peak decreases with the increase of the annealing temperature due to the increase in particle size and therefore an increase of the order of the interior of the lattice structure. Similar results were also observed by Wang et al. [37] and Kosacki et al. [38]. The broadband at around  $580\text{ cm}^{-1}$  is due to disorder in the oxygen sublattice (mainly VOs) [39]. In Figure 9(a), the deconvolution of this band in three ones can be seen; the mode at  $595\text{ cm}^{-1}$  is caused by VOs [40, 41]. The band located at  $560\text{ cm}^{-1}$  is due to the reduction of the lattice, since the desorption of oxygen originates the  $\text{Ce}^{3+}$  formation, producing the  $\text{Ce}^{3+}$ -VO complex [40, 42]. The third at  $\sim 620\text{ cm}^{-1}$  is related to the  $\text{SiO}_2$  from the glass substrate [43]. With regard to the

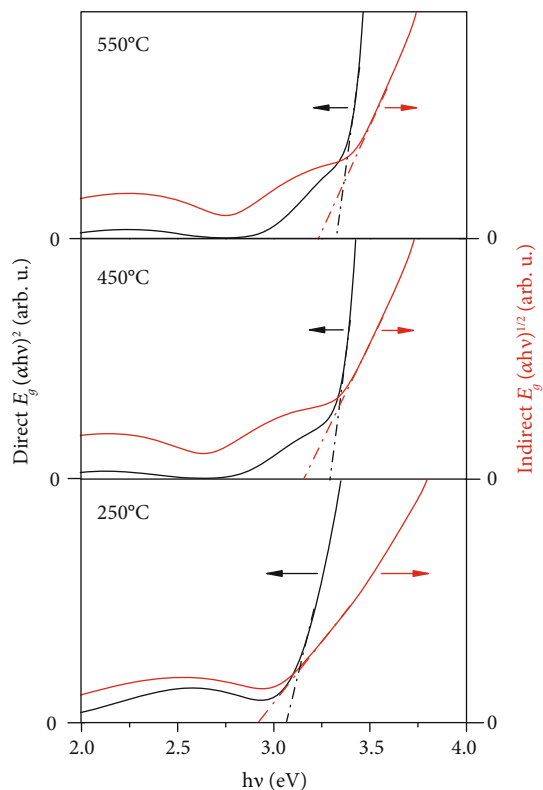


FIGURE 7: The plot of  $(\alpha h\nu)^2$  and  $(\alpha h\nu)^{1/2}$  versus photon energy for the films studied.

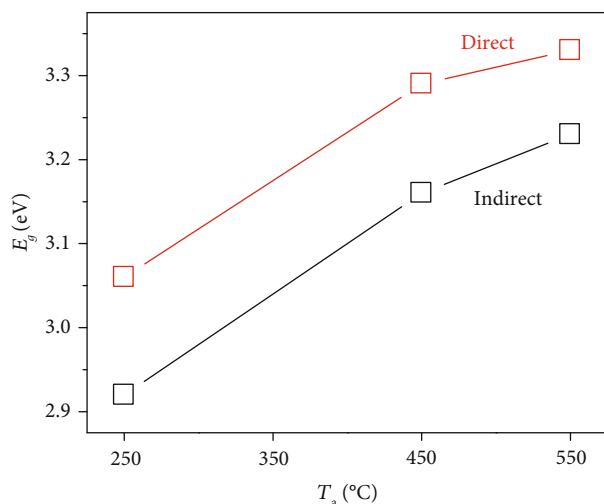


FIGURE 8:  $E_{gD}$  and  $E_{gI}$  as a function of the annealing temperature.

band at  $780\text{ cm}^{-1}$ , several authors have associated it with the presence of the  $^{18}\text{O}_2^+$  [40, 44].

Figure 9(b) displays in an augmented scale the frequency of the  $F_{2g}$  mode for the different  $T$ 's. This mode shifts to higher energies when  $T$  rises. Figure 9(c) exhibits the frequency of  $F_{2g}$  as a function of  $T$ . The mode hardens with  $T$  due to the strain provoked by the oxygen vacancies, whose density increases at the same time that  $T$  increases. This

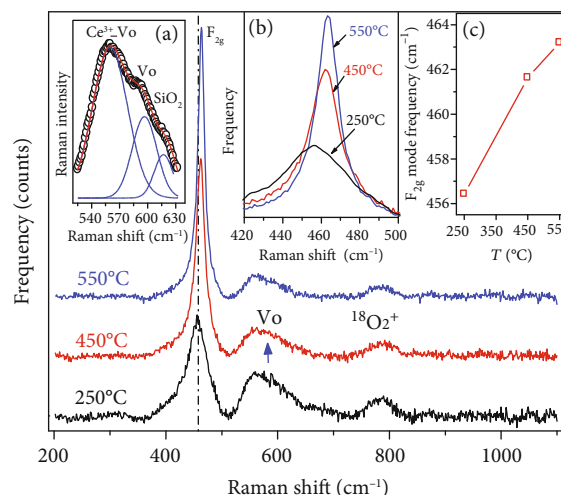


FIGURE 9: Raman spectra of  $\text{CeO}_2$  thin films annealed at the three temperatures studied. (a) Shows the shift of the  $F_{2g}$  mode. (c) Displays the frequency of the  $F_{2g}$  mode versus  $T$ .

result is consistent with those obtained by XRD, where larger  $T$  promotes a larger lattice contraction (see Figure 1), that is, increasing the stress on the atomic framework [45].

## 4. Conclusions

$\text{CeO}_2$  thin films have been synthesized successfully by the sol-gel dip-coating method. X-ray diffraction (XRD) results showed that all samples crystallized in the cubic fluorite structure and crystallinity increases with the increase of the annealing temperature. Crystallite size was found to be in the range  $4.0 \pm 0.5$  to  $11 \pm 1\text{ nm}$ , which increases as  $T$  augments. On the contrary, the interplanar (111) and (002) decrease when  $T$  rises. This behavior was explained by the strain in the films provoked by oxygen vacancies. The Raman peak at  $463\text{ cm}^{-1}$  indicates the  $F_{2g}$  active mode of the cerium cubic structure. A broad mode at  $590\text{ cm}^{-1}$  was deconvoluted in three ones: at  $560\text{ cm}^{-1}$  due to the  $\text{Ce}^{3+}$ -VO complex, at  $595\text{ cm}^{-1}$  associated to VOs, and at  $620\text{ cm}^{-1}$  assigned to the substrate. Based on SEM measurements, the films annealed at  $250^\circ\text{C}$  and  $450^\circ\text{C}$  show a densification process. The optical properties were also affected by  $T$  because an increase leads to an increase of both indirect and direct bandgap energy values.

## Data Availability

Data are available on request due to privacy/ethical restrictions. The data that support the findings of this study are available on request from the corresponding author (A. Méndez-López). The data are not publicly available due to restrictions, e.g., their containing information that could compromise the privacy of research participants.

## Conflicts of Interest

The authors declared that they have no conflicts of interest to this work.

## Acknowledgments

We appreciate the support of the “Programa para el Desarrollo Profesional Docente (PRODEP)” with the project “Concreto mejorado mediante el deposito de nanopartículas de ZrO<sub>2</sub>” and “Dirección de Planeación–Universidad Autónoma de Querétaro.” In addition, thanks are due to M. Sci. C. Zuñiga Romero, M. Sci. A. Tavira, M. Sci. A. Garcia Sotelo, M. Sci. A.B. Soto, Dr. R. Fragoso, Dr. J. Marquez Marin, Dr. A. Guillen, Eng. J.E. Urbina Alvarez, Eng. L.D. Guerrero-García, Eng. R.E. Aguilera-Perez, and Dr. M. Becerril for their technical assistance.

## References

- [1] A. Trovarelli, C. de Leitenburg, M. Boaro, and G. Dolcetti, “The utilization of ceria in industrial catalysis,” *Catalysis Today*, vol. 50, no. 2, pp. 353–367, 1999.
- [2] M. Mogensen, N. M. Sammes, and G. A. Tompsett, “Physical, chemical and electrochemical properties of pure and doped ceria,” *Solid State Ionics*, vol. 129, no. 1-4, pp. 63–94, 2000.
- [3] P. Nagaraju, Y. VijayaKumar, P. Radhika, R. J. Choudhary, and M. V. RamanaReddy, “Structural, morphological, optical and gas sensing properties of nanocrystalline ceria thin films,” *Materials Today: Proceedings*, vol. 3, 10, Part B, pp. 4009–4018, 2016.
- [4] L. Chaturvedi, S. Howlader, D. Chhikara, P. S. Deepak, S. Bagga, and K. M. K. Srivatsa, “Characteristics of nanocrystalline CeO<sub>2</sub> thin films deposited on different substrates at room temperature,” *Indian Journal of Pure & Applied Physics*, vol. 55, pp. 630–637, 2017.
- [5] A. K. Bhosale, N. L. Tarwal, P. S. Shinde et al., “Effective utilization of spray pyrolyzed CeO<sub>2</sub> as optically passive counter electrode for enhancing optical modulation of WO<sub>3</sub>,” *Solid State Ionics*, vol. 180, no. 23-25, pp. 1324–1331, 2009.
- [6] E. Kobayashi, Y. Watabe, T. Yamamoto, and Y. Yamada, “Cerium oxide and hydrogen co-doped indium oxide films for high-efficiency silicon heterojunction solar cells,” *Solar Energy Materials and Solar Cells*, vol. 149, pp. 75–80, 2016.
- [7] N. Izu, S. Nishizaki, T. Itoh, M. Nishibori, W. Shin, and I. Matsubara, “Gas response, response time and selectivity of a resistive CO sensor based on two connected CeO<sub>2</sub> thick films with various particle sizes,” *Sensors and Actuators B: Chemical*, vol. 136, no. 2, pp. 364–370, 2009.
- [8] P. Latha, R. Dhanabackialakshmi, P. S. Kumar, and S. Karuthapandian, “Synergistic effects of trouble free and 100% recoverable CeO<sub>2</sub>/nylon nanocomposite thin film for the photocatalytic degradation of organic contaminants,” *Separation and Purification Technology*, vol. 168, pp. 124–133, 2016.
- [9] J. B. R. Carvalho, R. S. Silva, I. Cesarino et al., “Influence of the annealing temperature and metal salt precursor on the structural characteristics and anti-corrosion barrier effect of CeO<sub>2</sub> sol-gel protective coatings of carbon steel,” *Ceramics International*, vol. 40, no. 8, pp. 13437–13446, 2014.
- [10] G. Balakrishnan, S. T. Sundari, P. Kuppusami et al., “A study of microstructural and optical properties of nanocrystalline ceria thin films prepared by pulsed laser deposition,” *Thin Solid Films*, vol. 519, no. 8, pp. 2520–2526, 2011.
- [11] I.-W. Park, J. Lin, J. J. Moore et al., “Grain growth and mechanical properties of CeO<sub>2-x</sub> films deposited on Si(100) substrates by pulsed dc magnetron sputtering,” *Surface and Coatings Technology*, vol. 217, pp. 34–38, 2013.
- [12] B. Elidrissi, M. Addou, M. Regragui, C. Monty, A. Bougrine, and A. Kachouane, “Structural and optical properties of CeO<sub>2</sub> thin films prepared by spray pyrolysis,” *Thin Solid Films*, vol. 379, no. 1-2, pp. 23–27, 2000.
- [13] J. de Souza, A. G. P. da Silva, and H. R. Paes Jr., “Synthesis and characterization of CeO<sub>2</sub> thin films deposited by spray pyrolysis,” *Journal of Materials Science: Materials in Electronics*, vol. 18, no. 9, pp. 951–956, 2007.
- [14] H.-G. Lee, Y.-M. Lee, C.-H. Jung, and G.-W. Hong, “Direct deposition of CeO<sub>2</sub> films on Ni metal substrate by chemical vapor deposition,” *Metals and Materials*, vol. 6, no. 3, pp. 261–265, 2000.
- [15] C. Goyenola, G. K. Gueorguiev, S. Stafström, and L. Hultman, “Fullerene-like CS<sub>x</sub>: a first-principles study of synthetic growth,” *Chemical Physics Letters*, vol. 506, no. 1-3, pp. 86–91, 2011.
- [16] R. S. Sonawane, B. B. Kale, and M. K. Dongare, “Preparation and photo-catalytic activity of Fe–TiO<sub>2</sub> thin films prepared by sol-gel dip coating,” *Materials Chemistry and Physics*, vol. 85, no. 1, pp. 52–57, 2004.
- [17] M. Yazıcı, O. Çomaklı, T. Yetim, A. F. Yetim, and A. Çelik, “Effect of sol aging time on the wear properties of TiO<sub>2</sub>-SiO<sub>2</sub> composite films prepared by a sol-gel method,” *Tribology International*, vol. 104, pp. 175–182, 2016.
- [18] K. Wang, Y. Chang, L. Lv, and Y. Long, “Effect of annealing temperature on oxygen vacancy concentrations of nanocrystalline CeO<sub>2</sub> film,” *Applied Surface Science*, vol. 351, pp. 164–168, 2015.
- [19] A. Verma, A. K. Bakhshi, and S. A. Agnihotry, “Effect of citric acid on properties of CeO<sub>2</sub> films for electrochromic windows,” *Solar Energy Materials and Solar Cells*, vol. 90, no. 11, pp. 1640–1655, 2006.
- [20] I. K. Škofic, S. Šturm, M. Čeh, and N. Bukovec, “CeO<sub>2</sub> thin films obtained by sol-gel deposition and annealed in air or argon,” *Thin Solid Films*, vol. 422, no. 1-2, pp. 170–175, 2002.
- [21] A. Kossoy, A. I. Frenkel, Y. Feldman, E. Wachtel, A. Milner, and I. Lubomirsky, “The origin of elastic anomalies in thin films of oxygen deficient ceria, CeO<sub>2-x</sub>,” *Solid State Ionics*, vol. 181, no. 33-34, pp. 1473–1477, 2010.
- [22] J. C. Nie, Z. Y. Hua, R. F. Dou, and Q. Y. Tu, “Quantum confinement effect in high quality nanostructured CeO<sub>2</sub> thin films,” *Journal of Applied Physics*, vol. 103, no. 5, article 054308, 2008.
- [23] Y. Zhou, Z. Wang, P. Yang et al., “Tensile strain switched ferromagnetism in layered NbS<sub>2</sub> and NbSe<sub>2</sub>,” *ACS Nano*, vol. 6, no. 11, pp. 9727–9736, 2012.
- [24] R. N. Bharathi and S. Sankar, “Structural, optical, and magnetic properties of Nd-doped CeO<sub>2</sub> nanoparticles codoped with transition metal elements (Cu, Zn, Cr),” *Journal of Superconductivity and Novel Magnetism*, vol. 31, no. 8, pp. 2603–2615, 2018.
- [25] A. Monshi, M. R. Foroughi, and M. R. Monshi, “Modified Scherrer equation to estimate more accurately nanocrystallite size using XRD,” *World Journal of Nano Science and Engineering*, vol. 02, no. 03, pp. 154–160, 2012.
- [26] B. B. Patil and S. H. Pawar, “Structural, morphological and electrical properties of spray deposited nano-crystalline CeO<sub>2</sub> thin films,” *Journal of Alloys and Compounds*, vol. 509, no. 2, pp. 414–420, 2011.

- [27] V. Mihalache and I. Pasuk, "Grain growth, microstructure and surface modification of textured CeO<sub>2</sub> thin films on Ni substrate," *Acta Materialia*, vol. 59, no. 12, pp. 4875–4885, 2011.
- [28] R. Suresh, V. Ponnuswamy, and R. Mariappan, "Impact of mole concentration on the structural and optical properties of nebulized spray coated cerium oxide thin films," *International Journal of Thin Films Science and Technology*, vol. 4, pp. 35–44, 2015.
- [29] C. W. M. Castleton, J. Kullgren, and K. Hermansson, "Tuning LDA+U for electron localization and structure at oxygen vacancies in ceria," *The Journal of Chemical Physics*, vol. 127, no. 24, p. 244704, 2007.
- [30] T. Désaunay, A. Ringuedé, M. Cassir, F. Labat, and C. Adamo, "Modeling basic components of solid oxide fuel cells using density functional theory: bulk and surface properties of CeO<sub>2</sub>," *Surface Science*, vol. 606, no. 3-4, pp. 305–311, 2012.
- [31] H. Shi, T. Hussain, R. Ahuja, T. W. Kang, and W. Luo, "Role of vacancies, light elements and rare-earth metals doping in CeO<sub>2</sub>," *Scientific Reports*, vol. 6, no. 1, article 31345, 2016.
- [32] Y.-W. Zhang, R. Si, C.-S. Liao, C.-H. Yan, C.-X. Xiao, and Y. Kou, "Facile alcohothermal synthesis, size-dependent ultraviolet absorption, and enhanced CO conversion activity of ceria nanocrystals," *The Journal of Physical Chemistry B*, vol. 107, no. 37, pp. 10159–10167, 2003.
- [33] A. Zarkov, A. Stanulis, L. Mikoliunaite et al., "Chemical solution deposition of pure and Gd-doped ceria thin films: structural, morphological and optical properties," *Ceramics International*, vol. 43, no. 5, pp. 4280–4287, 2017.
- [34] N. S. Arul, D. Mangalaraj, and J. I. Han, "Facile hydrothermal synthesis of CeO<sub>2</sub> nanopebbles," *Bulletin of Materials Science*, vol. 38, no. 5, pp. 1135–1139, 2015.
- [35] R. C. Deus, R. A. C. Amoresi, P. M. Desimone et al., "Electrical behavior of cerium dioxide films exposed to different gases atmospheres," *Ceramics International*, vol. 42, no. 13, pp. 15023–15029, 2016.
- [36] T. Hattori, K. Kobayashi, and M. Ozawa, "Size effect of Raman scattering on CeO<sub>2</sub> nanocrystal by hydrothermal method," *Japanese Journal of Applied Physics*, vol. 56, no. 1S, article 01AE06, 2017.
- [37] S. Wang, W. Wang, J. Zuo, and Y. Qian, "Study of the Raman spectrum of CeO<sub>2</sub> nanometer thin films," *Materials Chemistry and Physics*, vol. 68, no. 1-3, pp. 246–248, 2001.
- [38] I. Kosacki, T. Suzuki, H. U. Anderson, and P. Colomban, "Raman scattering and lattice defects in nanocrystalline CeO<sub>2</sub> thin films," *Solid State Ionics*, vol. 149, no. 1-2, pp. 99–105, 2002.
- [39] J. R. McBride, K. C. Hass, and B. D. Poindexter, "Evolution of microstructure in nanocrystalline Mo-Cu thin films during thermal annealing," *Journal of Applied Physics*, vol. 78, pp. 2435–2441, 1994.
- [40] Z. Wu, M. Li, J. Howe, H. M. Meyer, and S. H. Overbury, "Probing defect sites on CeO<sub>2</sub> nanocrystals with well-defined surface planes by Raman spectroscopy and O<sub>2</sub> adsorption," *Langmuir*, vol. 26, no. 21, pp. 16595–16606, 2010.
- [41] Y. Yang, Z. Mao, W. Huang et al., "Redox enzyme-mimicking activities of CeO<sub>2</sub> nanostructures: intrinsic influence of exposed facets," *Scientific Reports*, vol. 6, no. 1, article 35344, 2016.
- [42] M. Radović, B. Stojadinović, N. Tomić et al., "Investigation of surface defect states in CeO<sub>2</sub>-nanocrystals by scanning tunneling microscopy/spectroscopy and ellipsometry," *Journal of Applied Physics*, vol. 116, no. 23, pp. 234305–234308, 2014.
- [43] W. Lin, A. A. Herzing, C. J. Kiely, and I. E. Wachs, "Probing metal-support interactions under oxidizing and reducing conditions: in situ Raman and infrared spectroscopic and scanning transmission electron microscopic-X-ray energy-dispersive spectroscopic investigation of supported platinum catalysts," *Journal of Physical Chemistry C*, vol. 112, no. 15, pp. 5942–5951, 2008.
- [44] Y. M. Choi, H. Abernathy, H.-T. Chen, M. C. Lin, and M. Liu, "Characterization of O<sub>2</sub>-CeO<sub>2</sub> interactions using in situ Raman spectroscopy and first-principle calculations," *ChemPhysChem*, vol. 7, no. 9, pp. 1957–1963, 2006.
- [45] B. Choudhury, P. Chetri, and A. Choudhury, "Annealing temperature and oxygen-vacancy-dependent variation of lattice strain, band gap and luminescence properties of CeO<sub>2</sub> nanoparticles," *Journal of Experimental Nanoscience*, vol. 10, no. 2, pp. 103–114, 2013.

